A 64 × 64 SPAD Array for Portable Colorimetric Sensing, Fluorescence and X-Ray Imaging

Claudio Accarino, Gianluca Melino, Valerio Francesco Annese, Mohammed A. Al-Rawhani, Yash D. Shah, Dzmitry Maneuski, Christos Giagkoulovits, *Student Member, IEEE*, James P. Grant, Srinjoy Mitra, *Member, IEEE*, Craig Buttar, and David R. S. Cumming, *Fellow, IEEE*

***Abstract*— We present the design and application of a 64 x 64 pixel SPAD array to portable colorimetric sensing, and fluorescence and x-ray imaging. The device was fabricated on an unmodified 180 nm CMOS process and is based on a square p+/n active junction SPAD geometry suitable for detecting green fluorescence emission. The stand-alone SPAD shows a photodetection probability greater than 60% at 5 V excess bias, with a dark count rate of less than 4 cps/μm^2 and sub-ns timing jitter performance. It has a global shutter with an in-pixel 8-bit counter; four 5-bit decoders and two 64-to-1 multiplexer blocks allow the data to be read-out. The array of sensors was able to detect fluorescence from a fluorescein isothiocyanate (FITC) solution down to a concentration of 900 pM with an SNR of 9.8 dB. A colorimetric assay was performed on top of the sensor array with a limit of quantification of 3.1 μm. X-rays images, using energies ranging from 10 kVp to 100 kVp, of a lead grating mask were acquired without using a scintillation crystal.**

***Index Terms*— Single photon avalanche diode, SPAD, CMOS, low-light (vision), photo detector, image sensor, x-rays.**

I. Introduction

THE use of CMOS single photon avalanche diodes (SPADs) in biomedical sensing and imaging has increased as a consequence of their performance in terms of fast acquisition, high sensitivity and portability [1].Typical applications include fluorescence lifetime imaging microscopy (FLIM) [2]–[7], fluorescence [8], point-of-care testing (POCT) [9], Raman spectroscopy [10], positron emission tomography (PET) [11], endoscopic TOF PET [6], x-ray sensing [12], time-resolved spectroscopy [13], 3D vision and LIDAR [14]–[20], and quantum imaging [21]. All these applications require high sensitivity and extremely fast timing resolution of the order of picoseconds [22]. Additionally, SPADs are a suitable technology for portable imaging applications such as fluorescence endoscopic capsules [23], where low power consumption and small size are required.

SPADs with exceptionally low dark count rate (DCR), high photon detection probability and high dynamic range (DR) have been previously reported using customized enrichment layers manufactured in specialized CMOS technologies. Very high efficiency CMOS SPAD arrays with extremely complex on chip electronics, resulting in low fill factors have also been reported [24]. Exceptionally high DR values, larger than 100 dB, have been achieved using active quenching circuits to prevent saturation at high count rates, but at the expense of fill factor [25]. In such devices, microlenses are typically used to improve performance by concentrating light on to the active area, increasing the light capture by up to a factor of 10 [26] hence enhancing the optical fill factor [27]. This method can lead to misalignment and illumination non-uniformity in the optics. Recently high resolution and high fill-factor arrays have been reported [28], [29], along with the capability of manufacturing SPADs using 3D stack technology [30].

In this paper we demonstrate an advance in the use of low-cost legacy CMOS technology and its application in several sensing imaging modalities where a SPAD array is especially well suited. We initially detail the performance of a single square shaped photo-carrier diffusion SPAD, implemented on a test die, designed with a narrow depletion region and wide photon collection region to maximize the PDP. The SPAD was manufactured by AMS AG in a legacy unmodified 180 nm high voltage (HV) CMOS process. It achieves one of the lowest DCR at the 180 nm node, smaller than 4 cps/μm^2; this performance has been achieved without the need for any modification to the foundry process. The chips also have the highest PDP peak for any design using the 180 nm node; it is greater than 60% when operated at 5 V of excess bias.

Based on the figures of merit demonstrated by the stand-alone SPAD developed in the test chip we designed and implemented a 64 × 64 planar array (PA) for fluorescence, colorimetry, POCT and lab-on-a-chip (LoC) applications. The PA uses a global shutter with a digital 8-bit in-pixel counter, with data read-out circuits consisting of four 5-bit decoders and two 64-to-1 multiplexers. The resulting pixel pitch of 61.5 μm is a trade-off that is suitable for both the imaging and LoC

Manuscript received February 7, 2019; revised April 18, 2019; accepted May 4, 2019. Date of publication May 13, 2019; date of current version August 6, 2019. This work was supported by EPSRC CDT in Integrative Sensing and Measurement under Grant EP/L016753/1. Preliminary results, detailing the stand-alone SPAD design and characterization, were presented at the International Symposium on Circuits and Systems (ISCAS 2018), Florence, Italy, May 28, 2018. The associate editor coordinating the review of this paper and approving it for publication was Dr. Shoushun Chen. *(Corresponding author: Claudio Accarino.)*

C. Accarino, G. Melino, V. F. Annese, M. A. Al-Rawhani, C. Giagkoulovits, J. P. Grant, and D. R. S. Cumming are with the Microsystem and Technology Group, School of Engineering, University of Glasgow, Glasgow G128LT, U.K. (e-mail: c.accarino.1@research.gla.ac.uk; david.cumming.2@glasgow.ac.uk).

D. Maneuski and C. Buttar are with the Experimental Particle Physics Group, School of Physics and Astronomy, University of Glasgow, Glasgow G128LT, U.K.

Y. D. Shah was with the Microsystem Technology Group, University of Glasgow, Glasgow G128LT, U.K. He is now with the Extreme Light Group, University of Glasgow, Glasgow G128LT, U.K.

S. Mitra was with the University of Glasgow, Glasgow G128LT, U.K. He is now with The University of Edinburgh, Edinburgh EH93JW, U.K.

Digital Object Identifier 10.1109/JSEN.2019.2916424

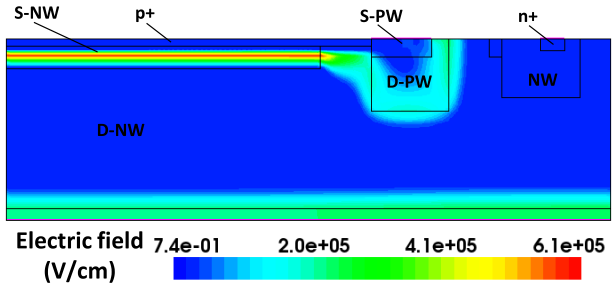

Fig. 1. Electric field profile of the SPAD at breakdown, simulated using Sentaurus TCAD.

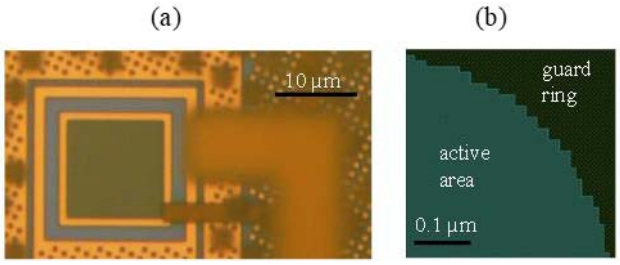

Fig. 2. (a) optical micrograph of the manufactured SPAD and (b) schematic detailing the smoothed guard ring.

applications; the former requires low pitch and high resolution whilst the latter requires space to potentially integrate fluidic microstructures.

As a proof of concept, we have demonstrated three different applications based on the SPAD PA: fluorescence imaging; x-ray imaging; and a colorimetric assay.

In sections II and III the design and characterization of a stand-alone SPAD are reported. In section IV we present the design, characterization and results from the 64 × 64 SPAD array. In section V we demonstrate three applications based on the 64 × 64 array.

II. Stand-Alone SPAD Design

The device is based on a square shaped p+ to shallow n-well (S-NW) active junction with smoothed corners. A low grading p-well guard ring protects the active junction whilst also acting as the anode and forming a secondary junction with the deep n-well (D-NW). The S-NW acts as an electric field enhancer for the active junction [31] whilst the guard ring is formed by implanting a shallow p-well (S-PW) into a deep p-well (D-PW). This guard ring configuration prevents an abrupt change of the doping profile and minimizes the guard ring size. The D-NW acts as the photo-collection region, allowing photo-generated electrons to diffuse into the avalanche region. The cathode is made of n+ into a n-well (NW). The cross section of the SPAD layout is illustrated in Fig. 1 along with the simulated electric field at breakdown. Fig. 2(a) shows a micrograph of the fabricated device, whilst Fig. 2(b) shows a close-up schematic of the curved guard ring. The side dimension of the effective active area is 11.6 μm and the cathode-to-cathode distance is 20.4 μm.

The curved guard ring, aiming at alleviating early breakdown, has a radius of curvature of 0.35 μm. This layer configuration was designed to achieve the maximum electric field at the active junction whilst minimizing the electric field value both in the guard ring and near to the guard ring. As can be seen in Fig. 1 a transition region at the edge of the guard ring is present in which the electric field slowly degrades.

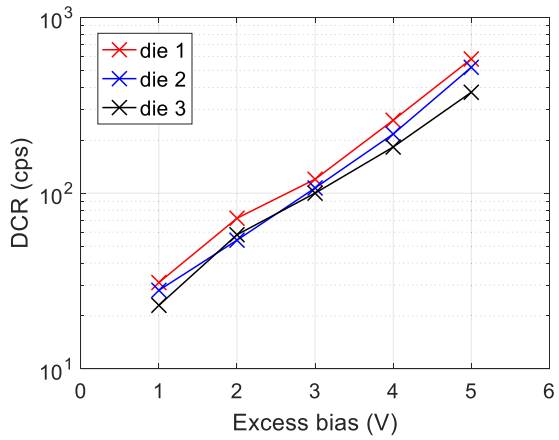

Fig. 3. DCR values versus excess bias voltage for three different die.

The maximum value of the electric field that is 600 kV/cm is achieved below the active junction whilst the guard ring junction presents a smoother electric field profile with electric fields in the range 100 to 236 kV/cm. This electric field profile allows for an improved detection efficiency whilst maximizing the breakdown difference between the main junction and the guard ring junction.

The parameters used in the simulation were calculated based on the average sheet resistance of the implants provided in the foundry documentation. The square shaped active area geometry was chosen to maximize the active area and the detection efficiency, since this active area is 1.2 times larger than a circular shaped geometry with same cathode to cathode distance.

III. Stand-Alone SPAD Characterization

The device, manufactured on a test die, showed a breakdown voltage of 16.8 V when tested with an external passive quenching circuit that used a 100 kΩ resistance. The DCR, PDP, and dead time were measured.

A. Dark Count Rate

DCR is the number of events a SPAD counts in the absence of light due to thermal agitation and the band-to-band tunneling effect [32]. It represents the base level of noise.

Fig. 3 shows the curve of the average DCR against excess voltage bias obtained from 3 different test die at room temperature (25°C). The data was acquired using a Keysight InfiniiVision MSO X 3054T oscilloscope, with statistical analysis capabilities, for an acquisition time of 2 minutes.

Fig. 4 shows the DCR temperature dependent behavior for the device under test (DUT) operated at different excess voltage biases with a dead time of 10 μ s. The DUT was placed in an environmental chamber, ensuring the total absence of light, and the temperature varied from 10 °C to 40 °C in 5 °C steps.

The voltage applied to the DUT was adjusted according to the temperature, to compensate for the temperature induced

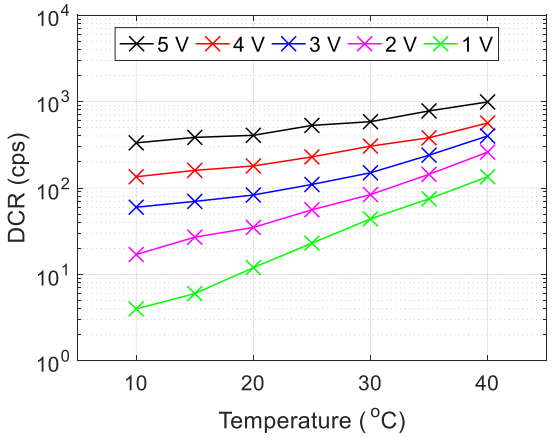

Fig. 4. DCR temperature behavior at different excess bias voltages.

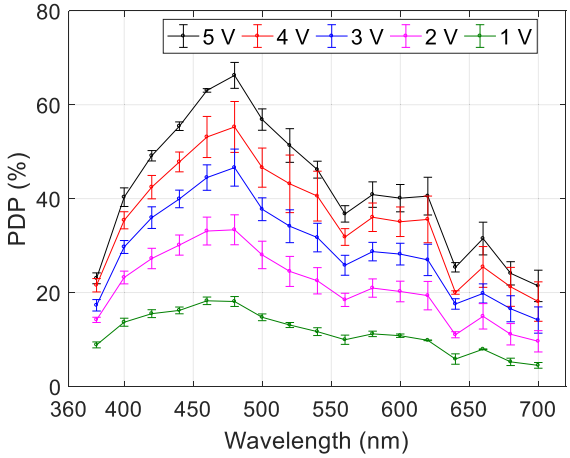

Fig. 5. Visible light PDP at different excess voltage biases along with the error bar values.

drift in breakdown, thus maintain a constant excess bias voltage. The minimum DCR value of 4 cps was observed at 1 V of excess bias at 10 °C, whilst the maximum DCR value of 1 kcps was measured at 5 V of excess bias at a temperature of 40 °C.

All the reported curves show similar trends. The DCR is sensitive to both excess bias voltage and temperature; of these sensitivity to voltage is dominant. Based on this observation we can conclude that the reverse bias current is dominated by band to band tunneling.

B. Photon Detection Probability

PDP is defined as the ratio between the number of incoming photons triggering an avalanche and the total number of photons illuminating the sensor at a selected wavelength in the span of the white light spectrum (380-760 nm) [32].

The experimental setup comprised a Hamamatsu L7893 Deuterium light source, a Jobin Yvon Horiba H20 series monochromator, and a Thorlabs IS200 integrating sphere connected by two optical fibers. Two sets of bi-convex lenses, Thorlabs LB1761-A, collimated the light from the optical sphere to the DUT and to a calibrated Hamamatsu S1336 photodiode. The monochromator, controlled by a computer, was tuned by adjusting the output wavelength in steps of 20 nm between 380 to 700 nm. The data, compensated for DCR, was acquired using a Keysight InfiniiVision MSO X 3054T oscilloscope, with statistical analysis capabilities, for an acquisition time of 2 minutes.

When the DUT was operated at 5 V of excess bias a PDP greater than 50% was measured from 440 to 520 nm with a peak of 65% at 480 nm, as reported in Fig. 5, along with PDP curves at lower excess biases. It can be noted that the 480 nm peak reduces to 55% when the DUT was operated at 4 V and to 48% at 3 V whilst it drastically reduces to 32% at 2 V. The reported curve is the average of two measurements and the error bars show the range of measurement. PDP is a function of doping levels, noise, excess bias and active area [33], therefore the obtained PDP is achieved thanks to the low noise of device, compared to other 180 nm HV SPADs which will have comparable doping levels, and a larger active area in lieu of the square shape. Fig. 6 shows a state-of-

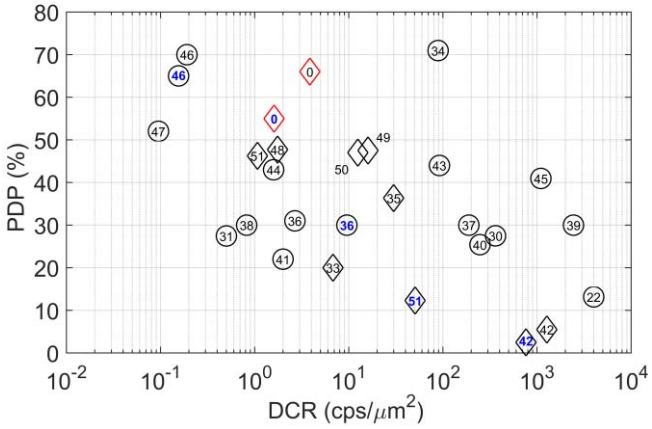

Fig. 6. PDP state-of-the-art, diamonds symbols highlight works at the 180 nm lithography nodes. Our device is reported in a red diamond symbols with a black number when operated at 5 V and a blue number when operated at 4 V. When a work is cited two times, the second citation is reported with a blue number.

the-art comparison in terms of DCR against PDP peak [22], [30], [31], [33]–[51], with diamond symbols denoting works in 180 nm lithography nodes and circle symbols for all the other nodes. For each symbol the corresponding reference number is inside the symbol (where possible). The same data, with the addition of the excess voltage bias and comments, are reported in Table I. For cases where works are reported twice to illustrate devices with different performances or relevant performances at different excess bias voltages, the second citation is reported with the corresponding reference number in blue, both in Fig. 6 and in Table I.

It can be easily noted that our device, when operated at both 4 V and 5 V, achieves the highest PDP peak in the 180 nm node, whilst in the same node the DCR value of our SPAD classifies second and forth lowest respectively.

Work in [33] reports similar DCR to the DCR value of our SPAD with a reduced PDP peak value. Our SPAD compared to the other works in the 180 nm node [35], [42] shows a higher PDP peak at a lower DCR value.

On a more general comparison our SPAD is outperformed by the work in [46] which achieves, with a 30 μm circular

TABLE I
PDP, DCR STATE-OF-THE-ART

Ref	DCR (cps/μm²)	PDP (%)	Vex (V)	Node (nm)	Note
[34]	89	70.9	12	130	n/a
[46]	0.19	70.0	9	160	30 μm SPAD C
0	3.86	66.0	5	180	**This work**
[46]	0.16	65.0	5	160	30 μm SPAD C
0	1.61	55.0	4	180	**This work**
[47]	0.10	52.0	6	350	n/a
[48]	1.75	47.7	3.3	180	n/a
[49]	16.00	47.5	4	180	n/a
[50]	12.48	47.0	10	180	n/a
[51]	1.07	46.3	8	180	Deep n-well/ p-epi SPAD
[43]	91.87	44.0	2.7	90	n/a
[44]	1.59	43.0	1	130	n/a
[45]	1100	40.9	2.7	130	n/a
[35]	30	36.3	2	180	n/a
[36]	2.68	31.0	6	150	10 μm SPAD
[37]	189	30.0	2	130	n/a
[36]	9.55	30.0	5.5	150	10 μm SPAD
[38]	0.82	30.0	4	150	n/a
[39]	2443.16	30.0	4.4	65	n/a
[30]	362.32	27.5	3	65	n/a
[31]	0.50	27.4	1.2	130	n/a
[40]	247.57	25.4	3	140	n/a
[41]	2	22.0	10.1	250	n/a
[33]	6.79	20.0	0.3	180	40 μm SPAD
[22]	4000	13.2	2.2	130	n/a
[51]	50.71	12.3	2.1	180	p+/n-well SPAD
[42]	1273.89	5.5	2	180	10 μm SPAD
[42]	764.33	2.5	0.5	180	10 μm SPAD

device, both the highest PDP peak and one of the lowest DCR in the state-of-the-art.

Work in [47] shows a comparable PDP peak with a much lower DCR whilst the work in [34] outperforms our PDP performance at the expense of the DCR value.

IV. ARRAY

A. Design

A micrograph of the 64 × 64 SPAD array chip, designed in the same technology node as the stand-alone SPAD, is presented in Fig. 7(a). The array, which is divided into 4 independent quadrants, has a global shutter architecture in order to optimize acquisition time and timing information. The

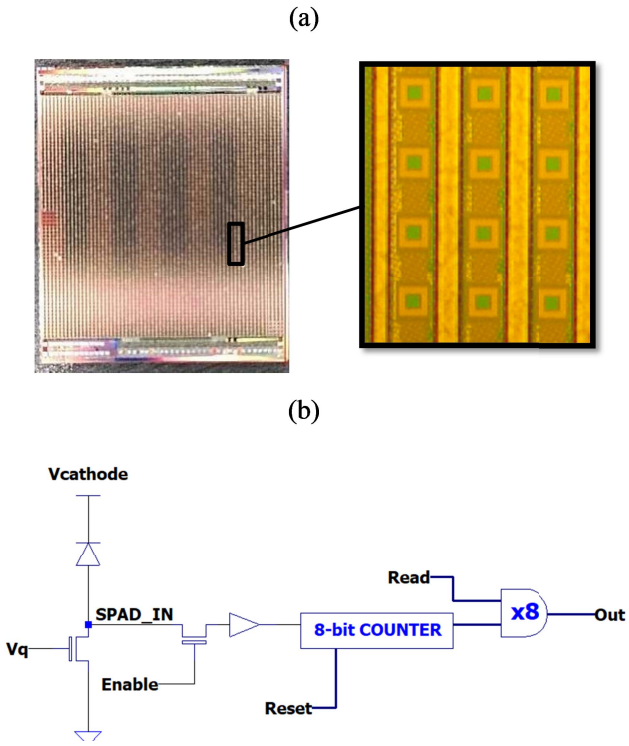

Fig. 7. (a) Optical Image of the 64 × 64 SPAD array, with inset of a 3x4 pixel section (b) in-pixel electronics diagram.

array has an 8-bit ripple counter per pixel and four independent 5-bit decoders (two vertical ones and two horizontal ones). It has two multiplexing systems, top and bottom, and a pitch size of 61.5 μm. The addressing of each quadrant is managed by a combination of a vertical and a horizontal decoder, whilst a cascade of a 32x1 multiplexer and 2x1 multiplexer handle the read-out process of each 8-bit pixel data count. The decoder and the multiplexing system may be activated either one at a time or sequentially allowing for a single quadrant or a combination of quadrants to be used at any time. A schematic of a pixel is shown in Fig. 7(b). Passive adjustable quenching of the SPAD is achieved with an NMOS whilst another NMOS connected to the global shutter allows the pulses to reach the 8-bit counting element. The read-out is controlled by an AND gate connected to the decoder inputs. Based on this architecture the SPAD excess bias can range from a minimum of 1.2 V to a maximum of 5 V whilst the chip supply voltage is 1.8 V.

B. Dark Count Rate Characterization

The chip was bonded to a 208 CPGA carrier, and a custom designed PCB for testing. An ST nucleo F338R8 MBED board, programmed to generate addressing pulses and to read count events from the chip, interfaces the chip to a laptop via a USB cable. We developed a Matlab code to synchronize and read the data on the serial port and then reconstruct the data into an image with a frame rate of 3 fps. The average breakdown voltage for the SPADs in the 64 × 64 array was 16.8 V, therefore a minimum bias of 18 V was required to acquire data. When the array was operated at 18 V with a shutter time of 1 ms the maximum power consumption was 100 mW.

TABLE II
DCR SUMMARY FOR THE 64 × 64 ARRAY

	18 V	19 V	20 V
Mean value (cps)	768	1972	3376
Median value (cps)	255	755	1453
Lower 50 % of array pixels (cps)	≤ 240	≤ 690	≤ 126
Lower 75 % of array pixels (cps)	≤ 400	≤ 1220	≤ 2270
Percentage below mean value (%)	88.7	85.6	83.9

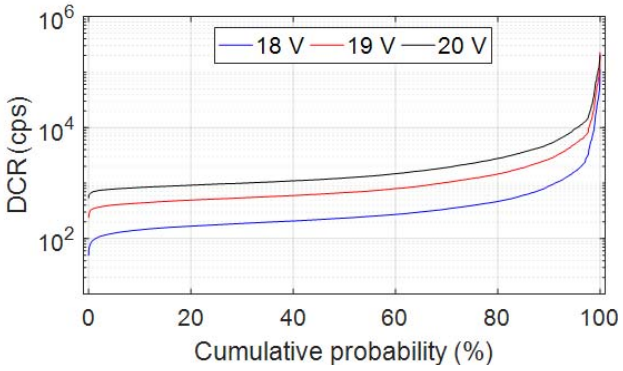

Fig. 8. Dark count rate cumulative probability for 18 V, 19 V and 20 V bias voltage at 25 °C.

Table II details the DCR statistics for bias voltages of 18 V, 19 V and 20 V at a temperature of 25 ° C. Fig. 8 shows the DCR cumulative probability at room temperature for the same three bias voltages of Table II.

For all bias voltages, more than 80% of the pixels show a DCR value smaller than the mean value as observed in the probability density functions and in the table. The reported mean DCR values are slightly higher than those of the single SPAD mainly because of the presence of hot pixels. The median value (where the effect of the hot pixels is less dominant) shows a significant reduction in the DCR.

C. Image Resolution

The image acquisition capability of the 64 × 64 SPAD array was tested by acquiring images in transmission mode through an optical block mounted on a 30 mm cage system comprising of three coated bi-convex lenses (Thorlabs LB1761-A), a green LED (LED TECHNOLOGY L02R3000F1), an iris (Thorlabs CP20S), and a black transmission mask. One lens, placed between the LED and the transmission mask, was used to achieve collimated light, whilst the other two were used to focus the light on the 64 × 64 SPAD array, which was mounted on an *xyz* translation stage for precision alignment.

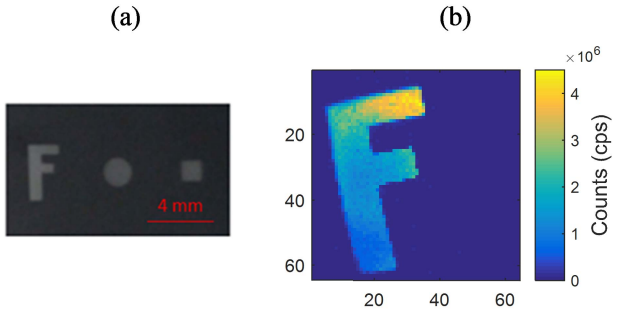

Fig. 9. (a) Picture of the custom-made transmission mask used in the setup. (b) Reconstructed image of the transmission mask.

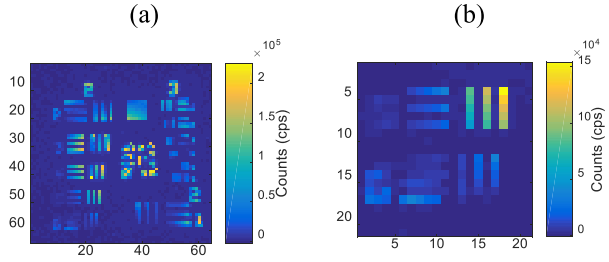

Fig. 10. (a) Acquired image of US AIR FORCE TARGET (Thorlabs R1DS1N). (b) Detail of the smallest resolved feature.

Fig. 9(a) shows the transmission mask, whilst Fig. 9(b) shows the acquired image of the transmission mask, taken with the 64 × 64 SPAD array with a voltage bias of 18 V, a shutter time of 100 μs and light power of 500 μW. As can be seen a low noise, high contrast image is obtained.

The spatial resolution of the 64 × 64 SPAD array was tested using the transmission setup, with a Thorlabs R1DS1N resolution target. Fig. 10(a) shows the acquired image of the target, and Fig. 10(b) shows the smallest resolved feature, which dictates the spatial resolution of the array. The smallest feature that is clearly resolved in both the x and y axis is 78.75 μm. The corresponding contrast for this feature was 94.4% and 85.7% in the x and y axis respectively.

V. APPLICATIONS

A. Fluorescence

Fluorescence experiments were performed on solutions of Fluorescein Isothiocyanate (FITC) at different concentrations. The used fluorescence setup comprised a LED (Thorlabs LED465E), collimating lens (Thorlabs 2x AC254-030-A-ML, 1 x AC254 075 A1 ML), blue excitation filter (Thorlabs MF475-35), green fluorescence emission filter (Thorlabs MF525-39), dichroic mirror (Thorlabs DMLP490L), and a 100 μm thick black transmission mask (Fig. 10(a)) taped to a small glass bottle containing the FITC solution. Only the F shaped aperture in the transmission mask was exposed to the excitation light whilst all the other apertures were sealed with black tape. The measured light power at the custom made mask position was 180 μW for a circular spot of 5 mm in diameter, the total transmitted power to the fluorophores is given by the ratio between the 'F' area and the circle area.

The experiments were conducted in three steps: a DCR image of the 64 × 64 SPAD array was acquired to evaluate the

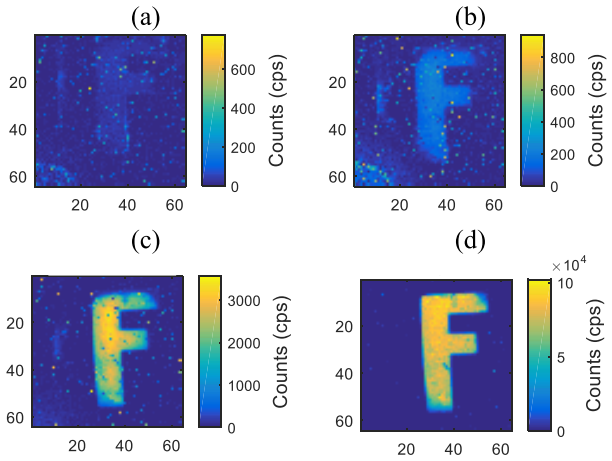

Fig. 11. (a) Control image with water (200 ms); Fluorescence images with FITC solutions of different concentrations: (b) 900 pM (200 ms), (c) 100 nM (50 ms) and (d) 100 μm (500 μ s). The corresponding SNR values are 3.6 dB, 9.8 dB, 19.66 dB and 26.86 dB.

base level of noise; the fluorescence image was acquired; and the DCR mask was subtracted from the fluorescence image. The FITC fluorophores, that have excitation and fluorescence wavelengths in the ranges 460-480 nm and 515 520 nm respectively, were purchased from Sigma Aldrich and dissolved in phosphate buffer saline to obtain solutions ranging from 100 μM to 900 pM concentrations of FITC.

The images in Fig. 11(a),(b),(c) and (d) were taken with different integration times and normalized in terms of counts per second. Different exposure times were used according to the image brightness, as state in the caption for Fig. 11. This was necessary so as to remain within the limit of the counter circuit. The control image with water has an SNR of 3.6 dB whilst the 900 pM FITC solution shows a value of 9.8 dB. This large difference validates detection of the fluorescence signal at sub-nM concentration. The SNR values at 100 nM is 19.66 dB whilst at 100 μm is 26.86 dB.

B. Colorimetric Sensing

A colorimetric assay employs specific reagents that undergo a measurable light absorbance change (at a specific wavelength) which is related to the concentration of the analyte under test.

Specifically, we present a colorimetric assay on chip for the quantification of sarcosine, a metabolite present in human body fluids, at three different concentrations: 5, 100 and 1000 μm respectively.

A specific enzyme, sarcosine oxidase (SaOx), reacts with sarcosine and produces hydrogen peroxide (H_2O_2):

$$sarcosine + H_2O + O_2 \overset{SaOx}{\Longrightarrow} formaldehyde + glycine + H_2O_2$$

The hydrogen peroxide is in turn used to oxidase a red dye (o-dianisidine) using a second enzyme (horseradish peroxidase, HRP):

$$H_2O_2 + reduced\text{o-dianisidine}\,(colorless) \overset{HRP}{\Longrightarrow} Oxidized\text{o-dianisidine}\,(brown)$$

When the concentration of HRP >> SaOx, it is assumed that the reaction rate of the chain is mainly dependent on the sarcosine reaction. This reaction rate is linked with the concentration of sarcosine, according to the Michaelis-Menten kinetics [52]:

$$v\,(t) = \frac{V_{max}[S\,(t)]}{K_m + [S\,(t)]} \tag{1}$$

where:

v(t) is the instantaneous reaction rate; V_{max} represents the maximum rate achieved by the system;

[S(t)] is the instantaneous concentration of the substrate (sarcosine in this specific case);

K_m is the Michaelis-Menten constant and represents the substrate concentration at which the rate of the reaction assumes a value equal to 50% of V_{max}.

Thus, by measuring the initial reaction rate (IRR), the initial concentration of the analyte under test can be estimated.

The experimental setup comprised a Bentahm light source, a Bentham TMc300 monochromator, and a Thorlabs IS200 integrating sphere. An iris (Thorlabs CP20S) and a bi-convex lens (Thorlabs LB1761-A) collimated light from the monochromator into the sphere, whilst two sets of bi-convex lenses (Thorlabs LB1761-A) collimated the light from the optical sphere to the DUT and to a calibrated photodiode (DH-Si Bentham).

A wavelength of 450 nm, corresponding to the absorption peak of the dye, was selected. The induced change in light transmission caused by the reaction was monitored by acquiring images with the DUT operated at 18 V and a shutter time of 500 μ s for a minimum number of frames of 6 minutes. The stability of the light source intensity was monitored using the calibrated photodiode.

A microfluidic channel was fabricated on the top of the PA using standard photolithography. All the reagents for the bioassay were purchased from Sigma-Aldrich.

After the images were corrected for DCR, the mean count value per channel during the experimental time was calculated and smoothed using second order exponential fitting. The IRR values for a control measurement with no SaOx and three different concentration of sarcosine are shown in in Fig. 12. Fig.12 also shown the limit of detetection ($LoD_{(cps/s)}$) and the limit of quantification ($LoQ_{(cps/s)}$) for sarcosine, calculated using Eq. (2) [53].

$$\begin{cases} LoD_{(cps/s)} = mean_{control} + 3.3std_{control} \\ LoQ_{(cps/s)} = mean_{control} + 10std_{control} \end{cases} \tag{2}$$

When the IRR value for the three concentration are fitted according to Eq. (1) the following values are obtained: V_{max} = 247.9 cps, K_m = 712 μm and an offset of 5.6.

Lastly, we converted the $LoD_{(cps/s)}$ and $LoQ_{(cps/s)}$ to concentrations values using Eq. (1), obtaining a $LoD_{(\mu M)}$ of 1 μm and a $LoQ_{(\mu M)}$of 3.1μM.

C. X-Ray

X-ray detection experiments were conducted with the 64 × 64 SPAD array, acquiring x-ray images of a lead grating

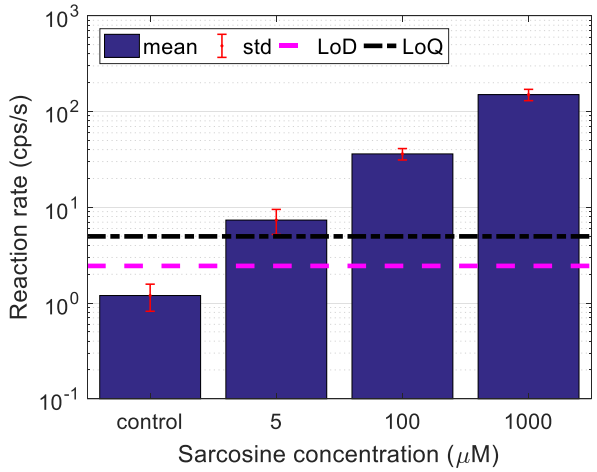

Fig. 12. IRR values for 5, 100, and 1000 μm of Sarcosine and control. The standard deviation values are reported in red, the LoD in a pink dashed line and the LoQ in a dotted black line.

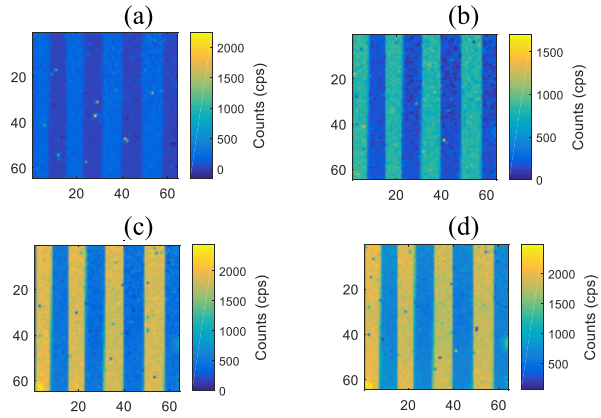

Fig. 13. X-ray images of the lead grating mask at different x-ray energies: (a) 20 kVp, (b) 30 kVp, (c) 50 kVp, and (d) 100 kVp. The SNRs were 9.7 dB, 7.4 dB, 6.2 dB and 4.6 dB respectively.

mask (PTW L659084). The test pattern was taped directly onto the 64×64 array which was then aligned to the x-ray tube. The experiment consisted of collecting frame data in three steps.

Frame 1: 10 DCR frames were measured and averaged.

Frame 2: 10 measurements with flood X-ray illumination of the array were measured and averaged.

Frame 3: the lead mask was attached to the array and 10 frames were measured and averaged.

Fig. 13 shows the result of combining Frame 1, 2, 3 to give a signal from Frame3-Frame2-Frame1. All the data used to produce Fig. 13 was taken with a shutter time of 50 ms, a cathode bias of 18 V, and an x-ray tube voltage from 20 kVp up to 100 kVp.

VI. Conclusion

We have reported a p+ to shallow n-well SPAD made in a legacy 180 nm HV CMOS technology with no modification.

The device has the highest PDP with the second lowest DCR (at 4 V excess voltage) from all 180 nm node devices reported in the literature. This stand-alone SPAD, operated at 5 V, shows a PDP higher than 50 % from 440 to 520 nm and a DCR less than 1 kcps. Based on these features the SPAD is particularly suited for applications such as portable fluorescence sensing under sub-nW/cm^2 illumination conditions. The device shows a good compromise between low DCR and high PDP. Using the new SPAD we developed a 64 × 64 SPAD array with an 8-bit ripple counter, 61.5 μm array pitch and 3.5% fill factor. For the array, the pixel had a median DCR of less than 2 kcps at room temperature at a bias voltage of 20 V. We successfully demonstrated the capability of the SPAD array to acquire fluorescence images of FITC at concentrations down to 900 pM with a minimum SNR of 9.8 dB. Moreover, we proved the capability of such a system to perform colorimetric assays on sarcosine in solution with a limit of quantification of 3.1 μm.

To the best of the authors' knowledge, this is the first reported SPAD array designed for visible light which is able to detect x-rays without a scintillation crystal.

The results we present show the utility of a readily available CMOS technology for advance sensing and imaging using single photon avalanche diodes.

Acknowledgment

The author is extremely grateful to Europractice for support during design and after fabrication.

The complete dataset can be found at http://dx.doi.org/10.5525/gla.researchdata.670

References

[1] Z. Cheng, X. Zheng, D. Palubiak, M. J. Deen, and H. Peng, "A comprehensive and accurate analytical SPAD model for circuit simulation," *IEEE Trans. Electron Devices*, vol. 63, no. 5, pp. 1940–1948, May 2016.

[2] D.-U. Li *et al.*, "Real-time fluorescence lifetime imaging system with a 32 × 32 013μm CMOS low dark-count single-photon avalanche diode array," *Opt. Express*, vol. 18, no. 10, pp. 10257–10269, 2010.

[3] L. Pancheri, N. Massari, and D. Stoppa, "SPAD image sensor with analog counting pixel for time-resolved fluorescence detection," *IEEE Trans. Electron Devices*, vol. 60, no. 10, pp. 3442–3449, Oct. 2013.

[4] D. Mosconi, D. Stoppa, L. Pancheri, L. Gonzo, and A. Simoni, "CMOS single-photon avalanche diode array for time-resolved fluorescence detection," in *Proc. 32nd Eur. Solid-State Circuits Conf.*, Sep. 2006, pp. 564–567.

[5] L. Pancheri and D. Stoppa, "A SPAD-based pixel linear array for high-speed time-gated fluorescence lifetime imaging," in *Proc. ESSCIRC*, Sep. 2009, pp. 428–431.

[6] A. Carimatto *et al.*, "A 67,392-SPAD PVTB-compensated multi-channel digital SiPM with 432 column-parallel 48ps 17b TDCs for endoscopic time-of-flight PET," in *Proc. IEEE Int. Solid-State Circuits Conf.*, Feb. 2015, pp. 202–203.

[7] L. Parmesan *et al.*, "A 256×256 SPAD array with in-pixel time to amplitude conversion for fluorescence lifetime imaging microscopy," in *Proc. Int. Image Sens. Workshop*, Jun. 2015, pp. 8–11.

[8] Y. Maruyama and E. Charbon, "A time-gated 128x128 CMOS SPAD array for on-chip fluorescence detection," in *Proc. Int. Image Sens. Workshop*, May 2011, pp. 270–273.

[9] Y. Maruyama, K. Sawada, H. Takao, and M. Ishida, "On-Chip multi wavelength detection sensor for real time monitoring of fluorescence and opacity," in *Proc. Int. Solid-State Sens., Actuators Microsyst. Conf.*, Jun. 2007, pp. 1971–1974.

[10] Y. Maruyama, J. Blacksberg, and E. Charbon, "A 1024 × 8, 700-ps time-gated SPAD line sensor for planetary surface exploration with laser Raman spectroscopy and LIBS," *IEEE J. Solid-State Circuits*, vol. 49, no. 1, pp. 179–189, Jan. 2014.

[11] J. R. Meijlink *et al.*, "First measurement of scintillation photon arrival statistics using a high-granularity solid-state photosensor enabling time-stamping of up to 20,480 single photons," in *Proc. IEEE Nucl. Sci. Symp. Conf. Rec.*, Oct. 2012, pp. 2254–2257.

[12] D. Renker and E. Lorenz, "Advances in solid state photon detectors," *J. Instrum.*, vol. 4, no. 4, 2009, Art. no. P04004.

[13] A. Kufcsák *et al.*, "Time-resolved spectroscopy at 19,000 lines per second using a CMOS SPAD line array enables advanced biophotonics applications," *Opt. Express*, vol. 25, no. 10, pp. 11103–11123, 2017.

[14] N. A. W. Dutton *et al.*, "A time-correlated single-photon-counting sensor with 14GS/S histogramming time-to-digital converter," in *Proc. IEEE Int. Solid-State Circuits Conf.*, Feb. 2015, pp. 204–205.

[15] N. A. W. Dutton *et al.*, "Oversampled ITOF imaging techniques using SPAD-based quanta image sensors," in *Proc. Int. Image Sensor Workshop*, Mar. 2015, pp. 1–4.

[16] C. L. Niclass, A. Rochas, P. A. Besse, and E. Charbon, "A CMOS single photon avalanche diode array for 3D imaging," in *Proc. IEEE Int. Solid-State Circuits Conf.*, Feb. 2004, pp. 120–517.

[17] C. Niclass, M. Soga, H. Matsubara, and S. Kato, "A 100-m range 10-frame/s 340 × 96-pixel time-of-flight depth sensor in 0.18-μmCMOS," in *Proc. Eur. Solid-State Circuits Conf.*, Jun. 2011, pp. 107–110.

[18] C. Niclass and E. Charbon, "A single photon detector array with 64×64 resolution and millimetric depth accuracy for 3D imaging," in *Proc. IEEE Int. Dig. Solid-State Circuits Conf.*, Feb. 2005, pp. 364–366.

[19] D. Stoppa *et al.*, "A 32x32-pixel array with in-pixel photon counting and arrival time measurement in the analog domain," in *Proc. ESSCIRC*, Sep. 2009, pp. 204–207.

[20] M. Gersbach *et al.*, "A parallel 32 × 32 time-to-digital converter array fabricated in a 130 nm imaging CMOS technology," in *Proc. ESSCIRC*, Sep. 2009, pp. 196–199.

[21] L. Gasparini *et al.*, "A 32 × 32-pixel time-resolved single-photon image sensor with 44.64μm pitch and 19.48% fill-factor with on-chip row/frame skipping features reaching 800kHz observation rate for quantum physics applications," in *Proc. IEEE Int. Solid-State Circuits Conf.*, Feb. 2018, pp. 98–100.

[22] D. Palubiak, M. M. El-Desouki, O. Marinov, M. J. Deen, and Q. Fang, "High-speed, single-photon avalanche-photodiode imager for biomedical applications," *IEEE Sensors J.*, vol. 11, no. 10, pp. 2401–2412, Oct. 2011.

[23] M. A. Al-Rawhani, J. Beeley, and D. R. S. Cumming, "Wireless fluorescence capsule for endoscopy using single photon-based detection," *Sci. Rep.*, vol. 5, no. 1, Dec. 2015, Art. no. 18591.

[24] C. Veerappan *et al.*, "A 160 × 128 single-photon image sensor with on-pixel 55ps 10b time-to-digital converter," in *IEEE Int. Solid-State Circuits Conf. (ISSCC) Dig. Tech. Papers*, Feb. 2011, pp. 312–313.

[25] A. Eisele *et al.*, "185 MHz count rate 139 dB dynamic range single-photon avalanche diode with active quenching circuit in 130 nm CMOS technology," in *Proc. Int. Image Sens. Workshop*, Jun. 2011, pp. 278–280.

[26] J. M. Pavia, M. Wolf, and E. Charbon, "Measurement and modeling of microlenses fabricated on single-photon avalanche diode arrays for fill factor recovery," *Opt. Express*, vol. 22, no. 4, pp. 4202–4213, 2014.

[27] I. Gyongy *et al.*, "Cylindrical microlensing for enhanced collection efficiency of small pixel SPAD arrays in single-molecule localisation microscopy," *Opt. Express*, vol. 26, no. 3, pp. 2280–2291, 2018.

[28] A. C. Ulku *et al.*, "A 512 × 512 SPAD image sensor with integrated gating for Widefield FLIM," *IEEE J. Sel. Topics Quantum Electron.*, vol. 25, no. 1, pp. 1–12, Feb. 2018.

[29] I. Gyongy *et al.*, "256 × 256, 100 kfps, 61 Fill-factor time-resolved SPAD image sensor for microscopy applications," in *IEDM Tech. Dig.*, Dec. 2016, pp. 2–8.

[30] T. Al Abbas, N. A. W. Dutton, O. Almer, S. Pellegrini, Y. Henrion, and R. K. Henderson, "Backside illuminated SPAD image sensor with 7.83 μm pitch in 3D-stacked CMOS technology," in *IEDM Tech. Dig.*, Dec. 2017, pp. 8-1-1–8-1-4.

[31] J. A. Richardson, E. A. G. Webster, L. A. Grant, and R. K. Henderson, "Scaleable single-photon avalanche diode structures in nanometer CMOS technology," *IEEE Trans. Electron Devices*, vol. 58, no. 7, pp. 2028–2035, Jul. 2011.

[32] Y. Khasin, *Characterization of Single Photon Avalanche Diode in CMOS Technology: Design and Characterization of a High Performance Single Photon Avalanche Diode in Standard CMOS Technology*, Lap Lambert Academic Publishing, Jan. 2014.

[33] I. Malass, W. Uhring, J. P. Le Normand, N. Dumas, and F. Dadouche, "Evaluation of size influence on performance figures of a single photon avalanche diode fabricated in a 180 nm standard CMOS technology," *Analog Integr. Circuits Signal Process.*, vol. 89, no. 1, pp. 69–76, 2016.

[34] E. A. G. Webster, L. A. Grant, and R. K. Henderson, "A high-performance single-photon avalanche diode in 130-nm CMOS imaging technology," *IEEE Electron Device Lett.*, vol. 33, no. 11, pp. 1589–1591, Nov. 2012.

[35] S. Mandai, M. W. Fishburn, Y. Maruyama, and E. Charbon, "A wide spectral range single-photon avalanche diode fabricated in an advanced 180 nm CMOS technology," *Opt. Express*, vol. 20, no. 6, pp. 5849–5857, 2012.

[36] L. Pancheri and D. Stoppa, "Low-noise single photon avalanche diodes in 0.15 μm CMOS technology," in *Proc. Eur. Solid-State Device Res. Conf.*, Sep. 2011, pp. 179–182.

[37] M. Gersbach, C. Niclass, E. Charbon, J. Richardson, R. Henderson, and L. Grant, "A single photon detector implemented in a 130 nm CMOS imaging process," in *Proc. 38th Eur. Solid-State Device Res. Conf.*, Sep. 2008, pp. 270–273.

[38] H. Xu, L. Pancheri, G.-F. D. Betta, and D. Stoppa, "Design and characterization of a p+/n-well SPAD array in 150 nm CMOS process: Erratum," *Opt. Express*, vol. 25, no. 11, pp. 12765–12778, 2017.

[39] S. Lindner, S. Pellegrini, Y. Henrion, B. Rae, M. Wolf, and E. Charbon, "A high-PDE, backside-illuminated SPAD in 65/40-nm 3D IC CMOS pixel with cascoded passive quenching and active recharge," *IEEE Electron Device Lett.*, vol. 38, no. 11, pp. 1547–1550, Nov. 2017.

[40] M.-J. Lee, P. Sun, and E. Charbon, "A first single-photon avalanche diode fabricated in standard SOI CMOS technology with a full characterization of the device," *Opt. Express*, vol. 23, no. 10, pp. 13200–13209, 2015.

[41] J.-Y. Wu, S.-C. Li, F.-Z. Hsu, and S.-D. Lin, "Two-dimensional mapping of photon counts in low- noise SPAD," in *Proc. Int. Image Sensor Workshop*, Jun. 2013, pp. 1–4.

[42] N. Faramarzpour, M. J. Deen, S. Shirani, and Q. Fang, "Fully integrated single photon avalanche diode detector in standard CMOS 0.18-μm technology," *IEEE Trans. Electron Devices*, vol. 55, no. 3, pp. 760–767, Mar. 2008.

[43] E. A. G. Webster, J. A. Richardson, L. A. Grant, D. Renshaw, and R. K. Henderson, "A single-photon avalanche diode in 90-nm CMOS imaging technology with 44 photon detection efficiency at 690 nm," *IEEE Electron Device Lett.*, vol. 33, no. 5, pp. 694–696, May 2012.

[44] S. Pellegrini and B. Rae, "Fully industrialised single photon avalanche diodes," *Proc. SPIE Adv. Photon Counting Techn. XI*, vol. 10212, p. 102120D, May 2017.

[45] C. Niclass, M. Gersbach, R. Henderson, L. Grant, and E. Charbon, "A single photon avalanche diode implemented in 130-nm CMOS technology," *IEEE J. Sel. Topics Quantum Electron.*, vol. 13, no. 4, pp. 863–869, Jul./Aug. 2007.

[46] M. Sanzaro, P. Gattari, F. Villa, A. Tosi, G. Croce, and F. Zappa, "Single-photon avalanche diodes in a 0.16 μm BCD technology with sharp timing response and red-enhanced sensitivity," *IEEE J. Sel. Topics Quantum Electron.*, vol. 24, no. 2, pp. 1–9, Mar. 2018.

[47] D. Bronzi *et al.*, "Low-noise and large-area CMOS SPADs with timing response free from slow tails," in *Proc. Eur. Solid-State Device Res. Conf.*, Sep. 2012, pp. 230–233.

[48] T. Leitner *et al.*, "Measurements and simulations of low dark count rate single photon avalanche diode device in a low voltage 180-nm CMOS image sensor technology," *IEEE Trans. Electron Devices*, vol. 60, no. 6, pp. 1982–1988, Jun. 2013,

[49] C. Veerappan and E. Charbon, "CMOS SPAD based on photo-carrier diffusion achieving PDP >40 from 440 to 580 nm at 4 V excess bias," *IEEE Photon. Technol. Lett.*, vol. 27, no. 23, pp. 2445–2448, Dec. 1 2015.

[50] C. Veerappan and E. Charbon, "A substrate isolated CMOS SPAD enabling wide spectral response and low electrical crosstalk," *IEEE J. Sel. Topics Quantum Electron.*, vol. 20, no. 6, pp. 299–305, Dec. 2014.

[51] J. Borg, "Performance and spatial sensitivity variations of single-photon avalanche diodes manufactured in an image sensor CMOS process," *IEEE Electron Device Lett.*, vol. 36, no. 11, pp. 1118–1120, Nov. 2015.

[52] H. Bisswanger, *Enzyme Kinetics: Principles and Methods*, 3rd ed. Hoboken, NJ, USA: Wiley, 2002.

[53] G. L. Long and J. D. Winefordner, "Limit of detection. A closer look at the IUPAC definition," *Anal. Chem.*, vol. 55, no. 7, pp. 712A–724A, 1983.

Claudio Accarino received the M.Sc. degree in bio-medical engineering from the University of Strathclyde, Glasgow, U.K., in 2014. He is currently pursuing the Ph.D. degree in integrative sensing and measurements with the Microsystem Technology Group and the Centre for Doctoral Training in Integrative Sensing and Measurements, University of Glasgow, Glasgow.

His research interests include CMOS electronics, optoelectronics, and low-illumination imaging.

Gianluca Melino received the B.Sc. degree in biomedical engineering from the Magna Graecia University of Catanzaro in 2013 by defending his thesis on the subject of "Matlab recipes for understanding the flow of anesthetics in patients during surgery," the M.Sc. degree in materials science and engineering from the King Abdullah University of Science and Technology, Saudi Arabia, in 2015, conducting research on the subject of "Nanofabrication of Surface Enhanced Raman Spectroscopy Substrates for Single/Few Molecules Detection." He is currently pursuing the Ph.D. degree with the University of Glasgow, under the Centre for Doctoral Training in Intelligent Sensing and Measurements Programme.

Valerio Francesco Annese received the B.Eng. degree in electronic and telecommunication engineering and the M.Sc. (*magna cum laude*) degree in electronics engineering from the Technical University of Bari, Bari, Italy, in 2014 and 2016, respectively. Currently, he is working toward the Ph.D. degree in electronic and electrical engineering at the University of Glasgow, Glasgow, U.K., with the Microsystem Technology (MST) Group, where he is focusing on the development of a metabolomics-on-CMOS platform.

From 2014 to 2016, he was a Research Assistant at the Design of Integrated Systems Laboratory (DEISLab) at the Technical University of Bari, where he focused on BCI and cyber-physical systems.

Mohammed A. Al-Rawhani received the B.Sc. degree in electronics and telecommunication engineering from Amman University, Amman, Jordan, in 2004, and the M.Sc. degree in electrical and electronic engineering and the Ph.D. degree in electronic integration design for biomedical applications from the University of Glasgow, Glasgow, U.K., in 2007 and 2012, respectively.

His research interests include CMOS low and high-voltage analogue/mixed-signal integrated circuits and front-ends for optical sensing biomedical applications.

Yash D. Shah received the B.E. (Hons.) degree from Mumbai University, India, the M.S. degree from Northwestern University, USA, where he focused on 2DEG low temperature measurements with capacitive contacts, and the Ph.D. degree from the University of Cambridge, U.K., working on THz quantum cascade lasers design and fabrication.

He is currently a PDRA with the Xtreme Light Group, University of Glasgow, U.K., focusing on quantum optics and metasurfaces.

Dzmitry Maneuski received B.Sc. degree in applied physics, mathematics, and computer sciences from the Moscow Institute of Physics in Technology in 2006, and the Ph.D. degree in physics and astronomy from the University of Glasgow in 2009.

He is currently a Research Fellow with the Particle Physics Experimental Group, University of Glasgow. His research interests include innovative hybrid pixel and particle tracking detectors, CMOS imagers, and spectroscopic detectors. His research work covers novel technology development, applications and commercialization in broad range of areas from Wakefield accelerators and synchrotrons to new inner tracker of the ATLAS detector and the large hadron collider, and transmission/scanning electron microscopy.

Christos Giagkoulovits (S'16) received the B.Sc. degree in physics and the M.Sc. degree in electronics and communications (radio electronics) from the University of Patras, Patras, Greece, in 2011 and 2013, respectively, and the Ph.D. degree in electrical and electronic engineering from the University of Glasgow, Glasgow, in 2018.

He is currently a Post-Doctoral Research Assistant with the Microsystems Technology Group, University of Glasgow. His research interests include mixed-mode CMOS integrated circuits for biomedical applications, low cost and low power biological sensors with a focus in electrochemistry, sensor arrays, and microsystems for sustainable lifestyle applications.

James P. Grant received the B.Sc. and Ph.D. degrees in physics from the University of Glasgow, in 2002 and 2006, respectively. His Ph.D. investigated wide band gap semiconductors, such as GaN, SiC, and diamond as radiation hard detector materials.

In 2007, he transferred to the School of Engineering, University of Glasgow, where is currently a Post-Doctoral Research Fellow with the Microsystems Technology Group. His research interests include nanofabrication, metamaterial devices, plasmonics, terahertz systems, sensors and imaging, and CMOS electronics.

Srinjoy Mitra received the bachelor's degree from Calcutta, India, and the M.Tech. degree from the Indian Institute of Technology, Bombay, India, in 2003, and the Ph.D. degree from the Institute of Neuroinformatics (UNI), ETH Zurich, Switzerland, in 2008.

From 2008 to 2010, he was a Post-Doctoral Researcher with Johns Hopkins University, Baltimore, MD, USA. He then joined the Medical Electronics Team at imec, Belgium, as a Senior Scientist, until 2016. Then, he joined the Biomedical Engineering Division, University of Glasgow, Glasgow, U.K., as a Lecturer. His primary research interest is in designing novel mixed signal CMOS circuits for advancement in medical and neural electronics.

Craig Buttar received the B.Sc. degree in natural philosophy and the Ph.D. degree from the University of Glasgow, in 1984 and 1987, respectively.

He is currently a Professor of Experimental Particle Physics with the University of Glasgow. He has worked on the construction of silicon tracker for the ATLAS experiment at CERN. His research interests include the development of silicon tracking systems for future particle physics experiments.

David R. S. Cumming (M'97–SM'08–F'13) received the B.Eng. degree in electronic and electrical engineering from the University of Glasgow, Glasgow, U.K., and the Ph.D. degree from Cambridge University, Cambridge, U.K., in 1989 and 1993, respectively.

He currently leads the Microsystem Technology Group, School of Engineering, University of Glasgow, where he is a Co-Founder of its spin-out, Mode Diagnostics. His research on CMOS ion sensitive array technology has also been commercialized into the Ion Torrent next generation sequencing system.

Dr. Cumming was a recipient of the Royal Society Wolfson Merit Award.